RSC Advances

PAPER

View Article Online
View Journal | View Issue

Cite this: *RSC Adv.*, 2023, **13**, 1078

Crystal structures, phase transitions, and nuclear magnetic resonance of organic–inorganic hybrid $[NH_2(CH_3)_2]_2ZnBr_4$ crystals†

Ae Ran Lim *[ab]

Received 23rd October 2022
Accepted 16th December 2022

DOI: 10.1039/d2ra06697a

rsc.li/rsc-advances

Organic–inorganic hybrid $[NH_2(CH_3)_2]_2ZnBr_4$ crystals were grown *via* slow evaporation, and their monoclinic structure was determined using single-crystal X-ray diffraction (XRD). The two phase transition temperatures at 401 K (T_{C1}) and 436 K (T_{C2}) were defined using differential scanning calorimetry and powder XRD. In the nuclear magnetic resonance spectra, a small change was observed in the ^{1}H chemical shifts for NH_2, ^{13}C chemical shifts for CH_3, and ^{14}N resonance frequency for NH_2 near T_{C1}. ^{1}H spin-lattice relaxation times $T_{1\rho}$ and ^{13}C $T_{1\rho}$ for NH_2 and CH_3, respectively, rapidly decreased near T_{C1}, suggesting that energy was easily transferred. NH_2 in the $[NH_2(CH_3)_2]^+$ cation was significantly influenced by the surrounding environments of ^{1}H and ^{14}N, indicating a change in the N–H···Br hydrogen bond with the coordination geometry of the $ZnBr_4$ anion. These fundamental properties open efficient avenues for the development of organic–inorganic hybrids, thus qualifying them for practical applications.

1. Introduction

Interest in organic–inorganic hybrid compounds has been primarily associated with their various applications, such as in sensors, fuel and solar cells, light-emitting diodes, and light-emitting transistors.[1–4] Furthermore, the important applications for materials with organic–inorganic hybrid perovskite are also as ferroelectrics, dielectric switches, and optical switches.[5–12] $CH_3NH_3PbX_3$ ($X = Cl^-$, Br^-, I^-) thin-film photovoltaic devices have been used as solar cells,[13–18] but these materials readily decompose in humid air and are toxic because of the presence of Pb. Thus, it is necessary to develop lead-free hybrid perovskite solar cells. Two-dimensional compounds of $[NH_3(CH_2)_nNH_3]MX_4$ ($n = 1, 2, 3, \ldots$; $M = Mn^{2+}$, Co^{2+}, Cu^{2+}, Zn^{2+}, Cd^{2+}, Pb^{2+}, $X = Cl^-$, Br^-, I^-) and $[(C_nH_{2n+1}NH_3)]_2MX_4$ are examples of organic–inorganic hybrids that have recently attracted considerable attention.[19–26] In addition, the dimethylammonium tetrabromozincate(II), $[NH_2(CH_3)_2]_2ZnBr_4$, crystal is a member of the $[NH_2(CH_3)_2]_2MX_4$ family, which belongs to a group of A_2MX_4 types, where A^+ is a univalent cation, M^{2+} is a divalent transition metal, and X is a halogen.[27–36] These crystals undergo several structural phase transitions, often associated with the ordering of hydrogen bonds and related changes in the molecular dynamics of the $[NH_2(CH_3)_2]^+$ ions. The individual MX_4 tetrahedral anions in these materials are completely isolated and surrounded by organic $[NH_2(CH_3)_2]^+$ cations. These substances are expected to act as potential proton conductors *via* hydrogen bonds. The structure of $[NH_2(CH_3)_2]_2ZnBr_4$, at 291 K is monoclinic with space group $P2_1/c$, and its lattice parameters are $a = 8.706$ Å, $b = 11.956$ Å, $c = 16.289$ Å, $\beta = 121.84°$, and $Z = 4$.[37] At 150 K, the structure is monoclinic, similar to that at 300 K; however, the space group and lattice constants are $P2_1/n$ and $a = 8.5512$ Å, $b = 11.825$ Å, $c = 13.499$ Å, $\beta = 90.358°$, and $Z = 4$.[38] In the molecular unit, the $ZnBr_4$ anions are connected to the organic $[NH_2(CH_3)_2]^+$ cations through N–H···Br hydrogen bonds.

With reference to previous reports on $[NH_2(CH_3)_2]_2ZnBr_4$, Ishihara *et al.*[37] investigated ^{81}Br nuclear quadrupole resonance (NQR) frequencies with varying temperature. Four NQR resonance signals to the four Br atoms in the $ZnBr_4$ tetrahedron were obtained; their NQR peaks disappeared at temperatures above 355 K, and no evidence of a phase transition was observed between 77 and 350 K. In addition, the phase transition temperatures measured using differential scanning calorimetry (DSC) were 401 and 435 K, and the melting temperature was reported to be 459 K by Horiuchi *et al.*[39] Mahfoudh *et al.*[38] reported considerably small endothermic peaks at 281, 340, and 377 K and a large endothermic peak at 408 K between 250 and 420 K. Their conductive and dielectric properties were reported to be functions of temperature. Subsequently, Mahfoudh *et al.*[40] investigated the optical and dielectric properties of $[NH_2(CH_3)_2]_2ZnBr_4$. Although the structure, NQR spectrum, and phase transition temperatures have been reported, the

[a]*Graduate School of Carbon Convergence Engineering, Jeonju University, Jeonju 55069, Korea*

[b]*Department of Science Education, Jeonju University, Jeonju 55069, Korea. E-mail: aeranlim@hanmail.net; arlim@jj.ac.kr*

† Electronic supplementary information (ESI) available. See DOI: https://doi.org/10.1039/d2ra06697a

thermodynamic stability and molecular dynamics based on varying temperature have not been widely evaluated.

In this study, we aimed to grow $[NH_2(CH_3)_2]_2ZnBr_4$, which is possibly a proton conductor owing to the availability of hydrogen bonds. The crystal structures and phase transition temperatures of $[NH_2(CH_3)_2]_2ZnBr_4$ were determined using single-crystal X-ray diffraction (XRD), powder XRD, DSC, and differential thermal analysis (DTA). Thermogravimetry analysis (TGA) was performed to better understand the thermal properties of the samples. In addition, nuclear magnetic resonance (NMR) chemical shifts for ^1H, ^{13}C, and ^{14}N were investigated to understand the coordination geometry and molecular dynamics of the organic $[NH_2(CH_3)_2]^+$ cation near the phase transition temperature T_C. In addition, to elucidate the molecular motion and energy transfer, the spin-lattice relaxation time, $T_{1\rho}$, for ^1H and ^{13}C were measured and investigated according to the temperature change. Herein, changes in the coordination geometry according to changes in temperature are explained by the changes in the N–H···Br hydrogen bonds between the $[NH_2(CH_3)_2]^+$ cations and $ZnBr_4$ anions. Investigating the physicochemical properties of the phase transition mechanism can help expand the application scope of $[NH_2(CH_3)_2]_2ZnBr_4$ crystals.

2. Experimental

$[NH_2(CH_3)_2]_2ZnBr_4$ single crystals were grown *via* slow evaporation in a thermostat at 300 K using an aqueous solution containing $NH(CH_3)_2 \cdot HBr$ (Aldrich, USA) and $ZnBr_2$ (99.99%, Aldrich, USA) of 2 : 1. To obtain a homogeneous solution, the solution was stirred and heated and then filtered through a filter. Thereafter, colourless single crystals grew after a few weeks.

The lattice parameters of the $[NH_2(CH_3)_2]_2ZnBr_4$ crystal at 150 and 300 K were determined by single-crystal XRD at the Korea Basic Science Institute (KBSI) Seoul Western Center. A colourless crystal was mounted on a Bruker D8 Venture PHOTON III M14 diffractometer with a Mo-Kα radiation source and a nitrogen cold stream (223 K). Data was collected and integrated using SMART APEX3 (Bruker, 2016) and SAINT (Bruker, 2016). The absorption was corrected using the multi-scan method implemented in SADABS. The structure was solved using direct methods and refined by full-matrix least-squares on F2 using SHELXTL.[41] All non-hydrogen atoms were refined anisotropically and hydrogen atoms were added to their geometrically ideal positions. The powder XRD patterns were measured at several temperatures using an XRD system with a Mo-Kα radiation source.

DSC measurements were performed on the powder using a DSC 25 apparatus (TA Instruments, USA) at a heating rate of 10 K min^{-1} under a nitrogen gas atmosphere. A sample weighing 4.5 mg was used for temperature measurements between 200 and 570 K.

TGA and DTA experiments were conducted using a thermogravimetric analyser (TA Instruments, USA) at the same heating rate as that used for DSC from 300 to 873 K under nitrogen gas. Optical observations were performed using a Carl Zeiss microscope equipped with a Linkam THM-600 heating stage.

Magic-angle spinning (MAS) NMR chemical shifts and spin-lattice relaxation time $T_{1\rho}$ of the $[NH_2(CH_3)_2]_2ZnBr_4$ crystal were measured using a Bruker 400 MHz Avance II+ NMR spectrometer (Bruker, Germany) at KBSI. The Larmor frequency for the ^1H MAS NMR experiment was $\omega_o/2\pi = 400.13$ MHz, and that for ^{13}C MAS NMR was $\omega_o/2\pi = 100.61$ MHz. To minimise spinning sidebands, the MAS speeds for ^1H and ^{13}C were measured at 10 kHz. Tetramethylsilane (TMS) and NH_4NO_3 were used as standard materials for accurate NMR chemical shift measurements. $T_{1\rho}$ values were obtained using a $\pi/2-\tau$ pulse, followed by a spin-lock pulse of duration τ, and the $\pi/2$ pulse widths for ^1H and ^{13}C were measured using a previously published method.[38] NMR experiments were not feasible at higher temperatures because of the limitations of the instrument.

3. Results and discussion

3.1. Crystal structure and phase transition

Single-crystal XRD results for the $[NH_2(CH_3)_2]_2ZnBr_4$ crystals were obtained at 150 and 300 K. The crystal structure at the two temperatures were grown to a monoclinic structure with space

Table 1 Crystal data and structure refinement for $[NH_2(CH_3)_2]_2ZnBr_4$ at 150 and 300 K (the complete data are available in the CIF files)

Chemical formula	$C_4H_{16}N_2ZnBr_4$	$C_4H_{16}N_2ZnBr_4$
Weight	477.20	477.20
Crystal system	Monoclinic	Monoclinic
Space group	$P2_1/n$	$P2_1/n$
T (K)	150	300
a (Å)	8.6262 (3)	8.7140 (11)
b (Å)	11.9760 (4)	11.9709 (12)
c (Å)	13.6877 (5)	13.8563 (16)
β (°)	90.3690 (10)	90.513 (4)
Z	4	4
V (Å^3)	1414.01	1445.4
Radiation type	Mo-Kα	Mo-Kα
Wavelength (Å)	0.71073	0.71073
Reflections collected	26 223	31 613
Independent reflections	3503 ($R_{int} = 0.0559$)	3610 ($R_{int} = 0.0576$)
Goodness-of-fit on F^2	1.048	1.025
Final R indices [$I > 2$sigma(I)]	$R_1 = 0.0214$, w$R_2 = 0.0455$	$R_1 = 0.0312$, w$R_2 = 0.0685$
R indices (all data)	$R_1 = 0.0268$, w$R_2 = 0.0471$	$R_1 = 0.0444$, w$R_2 = 0.0738$

group $P2_1/n$. The lattice constants at 150 K are $a = 8.6262$ Å, $b = 11.9760$ Å, $c = 13.6877$ Å, $\beta = 90.3690°$, and $Z = 4$, and those at 300 K are $a = 8.7140$ Å, $b = 11.9709$ Å, $c = 13.8563$ Å, $\beta = 90.513°$, and $Z = 4$. At both temperatures, the structures, space groups, and lattice constants are almost identical. The results at 150 and 300 K in our study are consistent with those obtained at 150 K by Mahfoudh *et al.*,[40] but slightly different from those obtained at 300 K by Ishihara *et al.*[37] Table 1 shows the XRD data of the $[NH_2(CH_3)_2]_2ZnBr_4$ crystal at 150 and 300 K; the atomic numbering and thermal ellipsoids for each atom are shown in Fig. 1. The Zn atom is coordinated by four Br atoms, forming a nearly regular tetrahedron of $ZnBr_4$. The hydrogen atoms of each formula unit form N–H···Br hydrogen bonds. Here, the length of N–H is 0.89 Å, and that of H···Br is in the range of 2.5–3.1 Å, which is consistent with previously reported results.[37,38] The detailed crystallographic parameters at 150 and 300 K are presented in the ESI.†

DSC curves were obtained for the $[NH_2(CH_3)_2]_2ZnBr_4$ crystals at heating and cooling rates of 10 K min^{-1}. In terms of heating, three strong endothermic peaks are observed at 401, 436, and 459 K (Fig. 2). This result is consistent with the DSC data reported by Horiuchi *et al.*[39] The transition enthalpies (ΔH) obtained from the peak area for 401 and 436 K are 9.79 and 6.64 kJ mol^{-1}, respectively, whereas that for 459 K is 13.79 kJ mol^{-1}, which is determined using the same method. Furthermore, exothermic peaks attributed to cooling are observed at 313, 361, 386, and 421 K, and the resulting entropies are 0.74, 3.56, 2.21, and 13.07 kJ mol^{-1}, respectively. The phase transition during heating and cooling is irreversible.

To further interpret the three endothermic peaks, the powder XRD patterns of $[NH_2(CH_3)_2]_2ZnBr_4$ were measured at increasing temperatures. The results in the measuring range (2θ) of 5–60° are depicted in Fig. 3. The XRD powder patterns below 390 K (green) are slightly different from that recorded at 420 K (red); this difference is ascribed to T_{C1} (401 K), exhibiting a clear change in structure.

Furthermore, the XRD pattern recorded at 420 K is different from that recorded at 445 K, which is attributed to T_{C2} (436 K). Finally, when the temperature is increased to 490 K, the powder pattern exhibits a completely different appearance, specifically, a non-crystalline form. The appearance of a single crystal is observed as a final check using an optical polarizing microscope. The crystal exhibits colourless transparency without significant change until the temperature is increased from 300 to 450 K. Finally, the surface of the single crystal begins to melt at approximately 460 K. The phase transition and melting temperatures shown in the powder XRD results are in reasonable agreement with the endothermic peaks in the DSC curves. From the DSC, XRD, and polarising microscopy experiments, the phase transition and melting temperatures are defined as $T_{C1} = 401$ K, $T_{C2} = 436$ K, and $T_m = 459$ K, respectively. Based on the results of DSC, single-crystal XRD, and powder XRD experiments, the structure does not change at 281, 340, and 377 K. Therefore, phase transitions apparently do not occur at the three previously reported temperatures. More comprehensively, the difference in this result is presumably attributed to

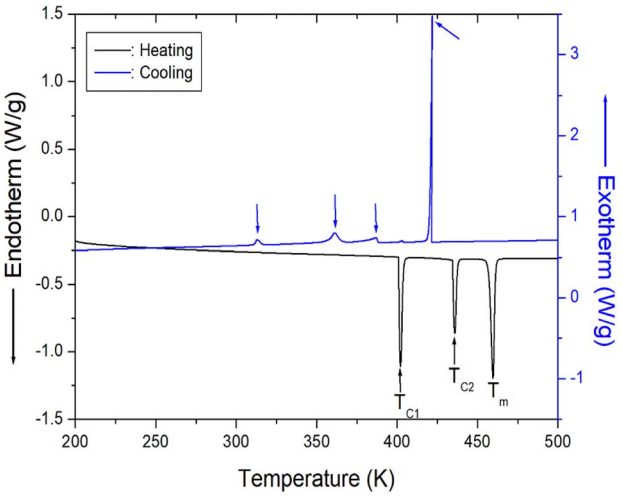

Fig. 2 Differential scanning calorimetry curve of $[NH_2(CH_3)_2]_2ZnBr_4$ crystal measured at heating and cooling speed of 10 K min^{-1}.

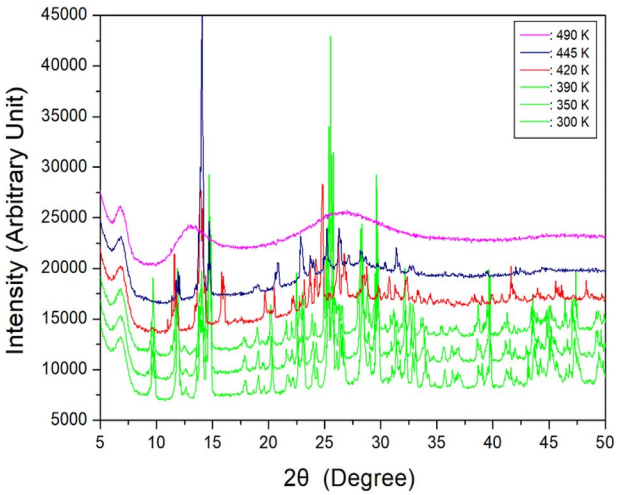

Fig. 3 Powder X-ray diffraction patterns of $[NH_2(CH_3)_2]_2ZnBr_4$ at 300, 350, 390, 420, 445, and 490 K.

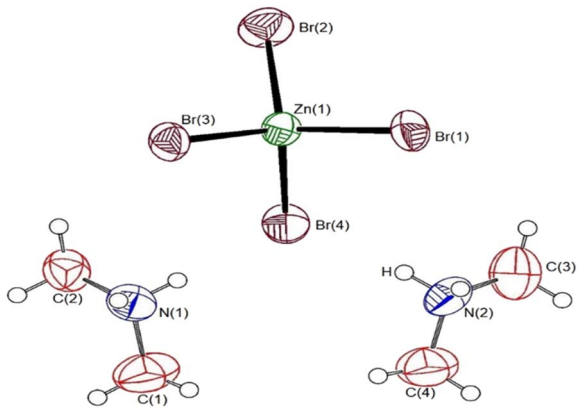

Fig. 1 Thermal ellipsoid plot (50% probability) for the $[NH_2(CH_3)_2]_2ZnBr_4$ structure at 300 K.

measurements performed under heating rate of 5 and 10 K min^{-1} during the DSC experiment. Moreover, a slight difference is considered to have occurred owing to the different basic reagents required for crystal growth.

3.2. Thermal properties

The TGA and DTA results obtained at a heating rate of 10 K min^{-1} are shown in Fig. 4. As the temperature is increased, the molecular weight of the $[NH_2(CH_3)_2]_2ZnBr_4$ crystals remains almost constant up to 550 K. The initial molecular weight loss is 2% at 560 K, and this temperature is defined as the partial thermal decomposition temperature, T_d. The molecular weight decreases sharply in the temperature range from 600 to 750 K, with a corresponding weight loss of 80% near 750 K, which is attributed to organic decomposition. Approximately 98% of the residual molecular weight is lost. Furthermore, the three endothermic peaks at 401, 436, and 459 K, shown in the DSC curve, are confirmed in the DTA curve.

3.3. ^1H and ^{13}C NMR chemical shifts and spin-lattice relaxation times

The ^1H NMR chemical shifts according to temperature change are shown in Fig. 5, and the two ^1H signals attributed to NH_2 and CH_3 in the cation structure are expressed in different colours. At 300 K, the ^1H chemical shift for NH_2 was recorded at 7.84 ppm, and that for CH_3 was obtained at 2.93 ppm. The ^1H chemical shifts for CH_3 are nearly independent of temperature, whereas those for NH_2 move in a slightly negative direction with increasing temperature. The surrounding environment of ^1H in NH_2 continuously changes with temperature, without an abrupt change near the phase transition temperature T_{C1}.

The ^{13}C chemical shifts in the MAS NMR spectra of $[NH_2(CH_3)_2]_2ZnBr_4$ with increasing temperature are shown in Fig. 6. The ^{13}C chemical shift for TMS as the standard reference at 300 K is recorded at 38.3 ppm, and this value is set to 0 ppm. Only the ^{13}C resonance line is recorded as one type of ^{13}C for the methyl carbons in the cation (inset of Fig. 6). The

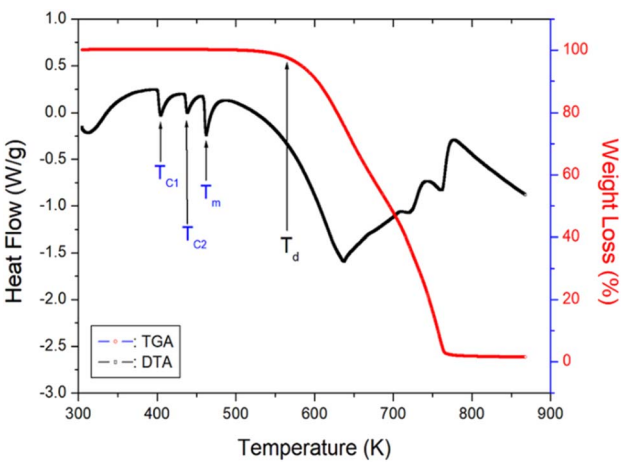

Fig. 4 Thermogravimetric analysis and differential thermal analysis curves of $[NH_2(CH_3)_2]_2ZnBr_4$.

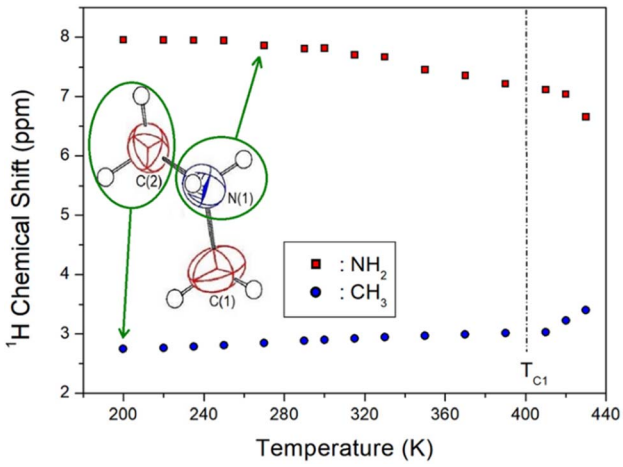

Fig. 5 ^1H nuclear magnetic resonance chemical shifts of NH_2 and CH_3 in $[NH_2(CH_3)_2]_2ZnBr_4$ based on the temperature change.

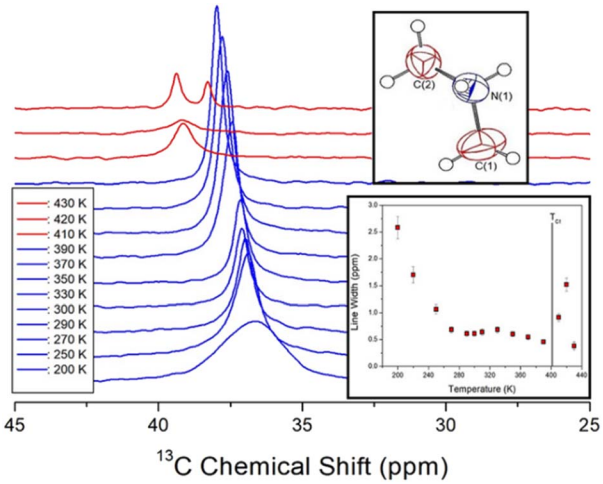

Fig. 6 *In situ* ^{13}C NMR spectra in $[NH_2(CH_3)_2]_2ZnBr_4$ for different temperatures (inset: change in line width for ^{13}C in $[NH_2(CH_3)_2]_2ZnBr_4$ with changing temperature).

^{13}C chemical shifts change more rapidly with temperature that those of ^1H. At 300 K, the ^{13}C chemical shift is recorded at 37.14 ppm, whereas that at 410 K above T_{C1} is discontinuously shifted to 39.12 ppm. In addition, at 430 K, which is close to T_{C2}, the NMR spectrum is separated into two resonance lines, showing chemical shifts of 39.36 and 38.28 ppm. The spectra below and above the phase transition temperature T_{C1} are depicted in blue and red, respectively. The chemical shifts of ^{13}C close to ^{14}N considerably change near T_{C1}, which implies that the environments surrounding ^{13}C change. The full-width at half-maximum for ^{13}C NMR spectra with respect to the temperature is shown in the inset of Fig. 6. The width of the resonance line is approximately 0.61 ppm at 300 K. As the temperature increases, the line width decreases rapidly, and that above T_{C1} is broadened again. The line width decreases with increasing temperature owing to internal molecular motion.

The ^{1}H and ^{13}C MAS NMR spectra were measured by changing the delay time at each temperature, and the plots of changes in intensity *versus* delay time were expressed as single-exponential functions. As shown in eqn (1), the reciprocal of the slope of the graph can be characterised as the spin-lattice relaxation time $T_{1\rho}$.[42–44]

$$I(\tau) = I(0)\exp(-\tau/T_{1\rho}) \quad (1)$$

where $I(\tau)$ and $I(0)$ are the signal intensities of the protons and carbons at times τ and $\tau = 0$, respectively. Decay curves for various delay times are measured, and their recovery traces exhibit different slopes at several temperatures. The ^{1}H $T_{1\rho}$ values are determined using eqn (1) for NH_2 and CH_3, and the ^{1}H $T_{1\rho}$ results as a function of 1000/temperature are shown in Fig. 7. The decay curves for carbon are also described by a single-exponential function to obtain ^{13}C $T_{1\rho}$ values. ^{1}H and ^{13}C $T_{1\rho}$ were measured with a spin-lock field of 73.53 kHz using the spin-locking pulse sequence method. From these results, the ^{13}C $T_{1\rho}$ values are obtained for methyl carbons as a function of 1000/temperature (Fig. 7).

The ^{1}H $T_{1\rho}$ values are strongly dependent on the temperature change; ^{1}H $T_{1\rho}$ of CH_3 above T_{C1} exhibits longer values than that of NH_2. An abruptly short value is observed above T_{C1}, and energy transfer is facilitated with abruptly short $T_{1\rho}$ values. ^{1}H $T_{1\rho}$ values for NH_2 and CH_3 decrease slightly with increasing temperature and increase again above 290 K. Below T_{C1}, the ^{1}H $T_{1\rho}$ values for CH_3 demonstrate a similar trend to that of the ^{1}H values for NH_2. In addition, the ^{13}C $T_{1\rho}$ values decrease with increasing temperature, similar to ^{1}H $T_{1\rho}$, and again increase above 250 K. At temperatures below T_{C1}, ^{13}C $T_{1\rho}$ values are approximately 10 times longer than ^{1}H $T_{1\rho}$. At temperatures below T_{C1}, the $T_{1\rho}$ values of ^{1}H and ^{13}C are minimum at 290 and 250 K, respectively, indicating molecular motion according to the Bloembergen–Purcell–Pound (BPP) theory. The $T_{1\rho}$ minimum is related to the re-orientational motion of NH_2 and CH_3 ions. The experimental value of $T_{1\rho}$ is expressed as the correlation time τ_C by the BPP theory, according to which $T_{1\rho}$ for molecular motion is given by:[34,35]

$$(1/T_{1\rho}) = C\,(\gamma_H^2\gamma_C^2\hbar^2/r^6)\{4\tau_C/[1+\omega_1^2\tau_C^2] + \tau_C/[1+(\omega_C-\omega_H)^2\tau_C^2] + 3\tau_C/[1+\omega_C^2\tau_C^2] + 6\tau_C/[1+(\omega_C+\omega_H)^2\tau_C^2] + 6\tau_C/[1+\omega_H^2\tau_C^2]\} \quad (2)$$

where C is a constant; γ_H and γ_C are the gyromagnetic ratios for protons and carbon, respectively; r is the distance of the H–C internucleus; ω_1 is the spin-lock field; ω_C and ω_H are the Larmor frequencies for carbon and protons, respectively. The data were analysed assuming that $T_{1\rho}$ was the minimum when $\omega_C\tau_C = 1$, and the relationship between $T_{1\rho}$ and ω_1 was applicable. As the $T_{1\rho}$ curves have a minimum value, coefficient C can be obtained using eqn (2). Using C, τ_C is calculated as a function of temperature. The local field fluctuation, according to the BPP theory, is attributed to the thermal motion of protons and carbons, which are activated by thermal energy. The correlation time τ_C of a motion follows Arrhenius behaviour, $\tau_C = \tau_C^{\circ}\exp(-E_a/k_BT)$, where τ_C° is the pre-correlation time, E_a is the activation energy of the molecular motions, and k_B is the Boltzmann constant.[36] The activation energy E_a depends on the molecular dynamics. To determine the molecular dynamics, τ_C is plotted against $1000/T$ on a logarithmic scale as shown in Fig. 8. The obtained values of E_a are 37.19 ± 1.66 kJ mol^{-1} for ^{1}H in NH_2, 31.87 ± 1.50 kJ mol^{-1} for ^{1}H in CH_3, and 21.67 ± 3.82 kJ mol^{-1} for ^{13}C in CH_3.

3.4. Static ^{14}N resonance frequency

The static NMR spectra of ^{14}N at the centre of the cation in the $[NH_2(CH_3)_2]_2ZnBr_4$ single crystal are shown in Fig. 9. Spectra in the temperature range of 200–420 K are obtained, and the direction of the applied magnetic field is measured with reference to the arbitrary direction of the single crystal. ^{14}N has a spin number of 1,[44] and two resonance signals are expected from the quadrupole interaction. The ^{14}N resonance frequency is extremely low at 28.90 MHz, and a resonance signal is not

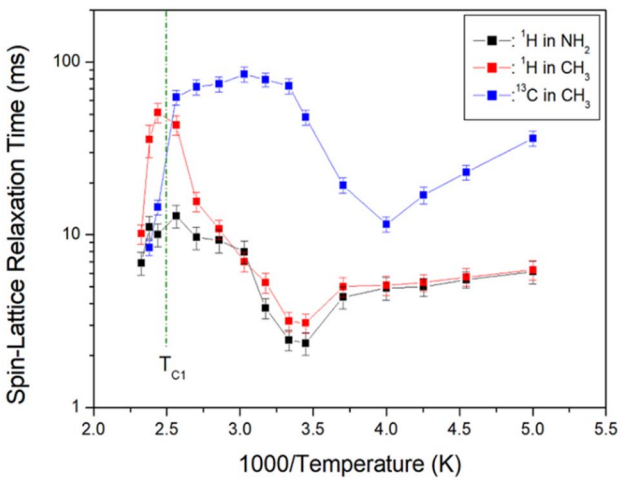

Fig. 7 ^{1}H and ^{13}C NMR spin-lattice relaxation times $T_{1\rho}$ in $[NH_2(CH_3)_2]_2ZnBr_4$ as functions of inverse temperature.

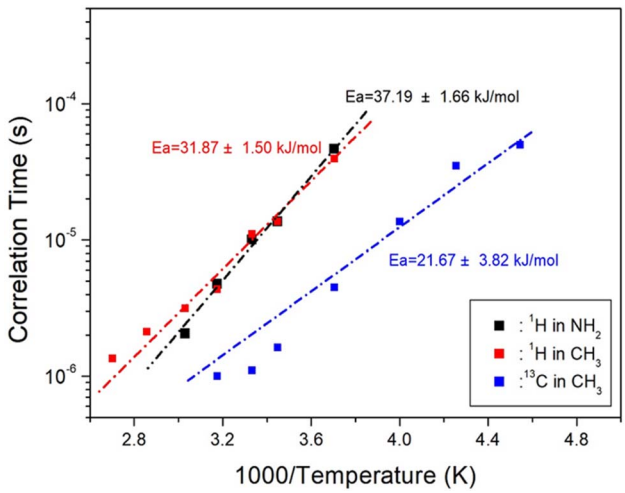

Fig. 8 Activation energies with correlation times for ^{1}H and ^{13}C in $[NH_2(CH_3)_2]_2ZnBr_4$ as functions of inverse temperature.

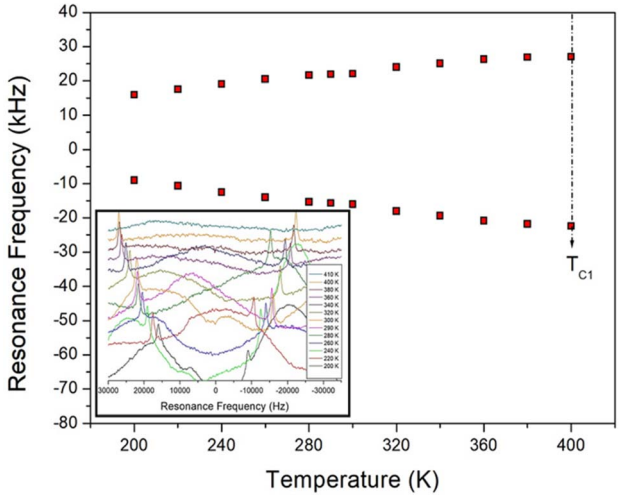

Fig. 9 Temperature dependence of ^{14}N resonance frequency in the $[NH_2(CH_3)_2]_2ZnBr_4$ crystal (inset: *in situ* ^{14}N NMR spectra of $[NH_2(CH_3)_2]_2ZnBr_4$ as a function of temperature).

easily obtained by wiggling the baseline (inset of Fig. 9). Owing to the low intensity and the relatively broad line width, the signals are not easily distinguished. The resonance frequencies of the ^{14}N NMR spectra are shown in Fig. 9 at several temperatures. Pairs for ^{14}N are indicated by symbols of the same colour.

The separation of two resonance lines increase slightly with increasing temperature. However, the ^{14}N NMR spectra disappear at temperatures near T_{C1} because of the re-orientational motion of $ZnBr_4$ tetrahedra and/or the thermal motion of the $[NH_2(CH_3)_2]^+$ cations. The continuous variation in the ^{14}N resonance frequency with changing temperature indicates a change in the coordination geometry of the environment around N.[45]

4. Conclusions

The crystal structure, phase transition, thermal stability, and molecular dynamics of $[NH_2(CH_3)_2]_2ZnBr_4$ crystals were investigated using XRD, DSC, TGA, and NMR. T_C values obtained from the DSC and XRD results were only 401 and 436 K, respectively, and single-crystal XRD results indicated that no phase transition occurred between 150 and 300 K. The peak at 459 K, as observed in the DSC experiment, was confirmed to be the melting temperature. The thermal stability was considerably high, with a thermal decomposition temperature of ~560 K. In the NMR spectra, changes were observed in the ^1H and ^{14}N chemical shifts for NH_2 and in the ^{13}C chemical shifts near T_{C1}, indicating changing structural environments. The environments of ^1H, ^{13}C, and ^{14}N located near NH_2 in the $[NH_2(CH_3)_2]^+$ cation significantly influenced it, thus indicating a change in the N–H···Br hydrogen bond with the coordination geometry of the $ZnBr_4$ anion. The ^1H $T_{1\rho}$ and ^{13}C $T_{1\rho}$ values decreased rapidly near T_{C1}, suggesting that energy transfer was facilitated. The increased variations in the ^1H NMR chemical shift and $T_{1\rho}$ of NH_2 in the cation with changes in temperature relative to those of CH_3 caused the significant change in the N–H···Br hydrogen bonding between the Br around Zn and H of NH_2. These fundamental properties open efficient avenues for the development of organic–inorganic hybrids, thus qualifying them for practical applications.

Author contributions

A. R. Lim performed NMR and X-ray experiments, and wrote the manuscript.

Conflicts of interest

There are no conflicts to declare.

Acknowledgements

This research was supported by the Basic Science Research Program of the National Research Foundation of Korea (NRF), funded by the Ministry of Education, Science, and Technology (2018R1D1A1B07041593 and 2016R1A6A1A03012069).

References

1 Y.-F. Gao, T. Zhang, W.-Y. Zhang, Q. Ye and F. Da-Wei, *J. Mater. Chem. C*, 2019, **7**, 9840.
2 Z.-X. Yu, P.-P. Zhang, W.-Y. Shi, Q. Y. Zhang and D.-W. Fu, *J. Phys. Chem. C*, 2019, **123**, 28385.
3 M. Mathlouthi, A. Valkonen, M. Rzaigui and W. Smirani, *Phase Transitions*, 2017, **90**, 399.
4 X.-N. Hua, J.-X. Gao, T. Zhang, X.-G. Chen, D.-S. Sun, Y.-Z. Zhang and W.-Q. Liao, *J. Phys. Chem. C*, 2019, **123**, 21161.
5 Z.-X. Wang, Y. Zhang, Y.-Y. Tang, P.-F. Li and R.-G. Xiong, *J. Am. Chem. Soc.*, 2019, **141**, 4372.
6 Z.-X. Wang, H. Zhang, F. Wang, H. Cheng, W.-H. He, Y.-H. Liu, X.-Q. Huang and P.-F. Li, *J. Am. Chem. Soc.*, 2020, **142**, 12857.
7 Y.-L. Zeng, X.-Q. Huang, C.-R. Huang, H. Zhang, F. Wang and Z.-X. Wang, *Angew. Chem., Int. Ed.*, 2021, **60**, 10730.
8 X.-G. Chen, X.-J. Song, Z.-X. Zhang, P.-F. Li, J.-Z. Ge, Y.-Y. Tang, J.-X. Gao, W.-Y. Zhang, D.-W. Fu, Y.-M. You and R.-G. Xiong, *J. Am. Chem. Soc.*, 2020, **142**, 1077.
9 M. Maczka, J. K. Zareba, A. Gagor, D. Stefanska, M. Ptak, K. Roleder, D. Kajewski, A. Soszynski, K. Fedoruk and A. Sieradzki, *Chem. Mater.*, 2021, **33**, 2331.
10 M. Maczka, M. Ptak, A. Gagor, D. Stefanska, J. K. Zareba and A. Sieradzki, *Chem. Mater.*, 2020, **32**, 1667.
11 K. Han, X. Ye, B. Li, Z. Wei, J. Wei, P. Wang and H. Cai, *Inorg. Chem.*, 2022, **61**, 11859.
12 H. Zhang, Y.-H. Tan, Y.-Z. Tang, X.-W. Fan, X.-L. Peng, R.-R. Han, Y.-K. Li and F.-X. Wang, *Inorg. Chem.*, 2022, **61**, 10454.
13 O. Knop, R. E. Wasylishen, M. A. White, T. S. Cameron and M. J. M. Van Oort, *Can. J. Chem.*, 1990, **68**, 412.

14 Q. Chen, N. D. Marco, Y. Yang, T.-B. Song, C.-C. Chen, H. Zhao, Z. Hong, H. Zhou and Y. Yang, *Nano Today*, 2015, **10**, 5.
15 I. M. Hermes, S. A. Bretschneider, V. W. Bergmann, D. Klasen, J. Mars, W. Tremel, F. Laquai, H.-J. Butt, M. Mezger, R. Berger, B. J. Rodriguez and S. A. L. Weber, *J. Phys. Chem.*, 2016, **120**, 5724.
16 E. Strelcov, Q. Dong, T. Li, J. Chae, Y. Shao, Y. Deng, A. Gruverman and J. Huang, *Sci. Adv.*, 2017, **3**, e1602165.
17 S. K. Abdel-Aal, A. S. Abdel-Rahman, G. G. Kocher-Oberlehner, A. Ionov and R. Mozhchil, *Acta Crystallogr., Sect. A: Found. Adv.*, 2017, **70**, C1116.
18 Y. Liu, L. Collins, R. Proksch, S. Kim, B. R. Watson, B. Doughty, T. R. Calhoun, M. Ahmadi, A. V. Ievlev, S. Jesse, S. T. Retterer, A. Belianinov, K. Xiao, J. Huang, B. G. Sumpter, V. Kalinin, B. Hu and O. S. Ovchinnikova, *Nat. Mater.*, 2018, **17**, 1013.
19 S. Gonzalez-Carrero, R. E. Galian and J. Perez-Prieto, *Part. Part. Syst. Charact.*, 2015, **32**, 709.
20 B. Staskiewicz, O. Czupinski and Z. Czapla, *J. Mol. Struct.*, 2014, **1074**, 723.
21 B. Staskiewicz, I. Turowska-Tyrk, J. Baran, C. Gorecki and Z. Czapla, *J. Phys. Chem. Solids*, 2014, **75**, 1305.
22 Z. Czapla, J. Przesławski, M. Crofton, J. Janczak, O. Czupinski, A. Ingram and M. Kostrzewa, *Phase Transitions*, 2017, **90**, 637.
23 S. K. Abdel-Aal, G. Kocher-Oberlehner, A. Ionov and R. N. Mozhchil, *Appl. Phys. A*, 2017, **123**, 531.
24 Y. Wei, P. Audebert, L. Galmiche, J. S. Lauret and E. Deleporte, *Materials*, 2014, **7**, 4789.
25 S. Ahmad, C. Hanmandlu, P. K. Kanaujia and G. V. Prakash, *Opt. Mater. Express*, 2014, **4**, 1313.
26 S. K. Abdel-Aal and A. S. Abdel-Rahman, *J. Cryst. Growth*, 2017, **457**, 282.
27 G. Vlokh, V. B. Kapustyanyk, I. I. Polovinko, S. A. Sveleba, V. M. Varikash and Z. A. Bobrova, *Appl. Spectrosc.*, 1990, **52**, 527.
28 V. I. Torgashev, Yu. I. Yuzyuk, L. M. Rabkin, Yu. I. Durnev and Z. A. Bobrova, *Phys. Status Solidi B*, 1991, **168**, 317.
29 I. I. Polovinko, S. A. Sveleba, V. Kapustianyk and V. S. Zhmurko, *Phys. Status Solidi A*, 1992, **131**, 13.
30 V. B. Kapustianik, I. I. Polovinko, S. A. Sveleba, O. G. Vlokh, Z. A. Bobrova and V. M. Varikash, *Phys. Status Solidi A*, 1992, **133**, 45.
31 V. Dzhala, V. Kapustianik, I. Kityk, I. Polovinko and S. Sveleba, *Ferroelectrics*, 1994, **152**, 273.
32 V. B. Kapustianik, H. Kabelka, H. Warhanek and A. Fuith, *Phys. Status Solidi A*, 1996, **155**, 95.
33 V. B. Kapustyanyk, *Appl. Spectrosc.*, 1998, **65**, 427.
34 N. H. Kim, J. H. Choi and A. R. Lim, *Solid State Sci.*, 2014, **38**, 103.
35 A. R. Lim and Y. Paik, *Solid State Sci.*, 2017, **65**, 61.
36 N. Mahfoudh, K. Karoui, M. Gargouri and A. BenRhaiem, *Appl. Organomet. Chem.*, 2020, **34**, e5404.
37 H. Ishihara, S.-q. Dou, K. Horiuchi, V. G. Krishnan, H. Paulus, H. Fuess and A. Weiss, *Z. Naurforsch. A*, 1996, **51**, 1027.
38 N. Mahfoudh, K. Karoui, F. Jomni and A. B. Rhaiem, *Appl. Organomet. Chem.*, 2020, **34**, e5656.
39 K. Horiuchi, H. Ishihara and H. Terao, *J. Phys.: Condens. Matter*, 2000, **12**, 4799.
40 N. Mahfoudh, K. Karoui and K. BenRhaiem, *RSC Adv.*, 2021, **11**, 24526.
41 M. Y. Choi, S. J. Lee, H. Ju and A. R. Lim, *RSC Adv.*, 2022, **12**, 20679.
42 A. R. Lim, *Sci. Rep.*, 2020, **10**, 20853.
43 A. Abragam, *The Principles of Nuclear Magnetism*, Oxford Univ. Press, 1961.
44 J. L. Koenig, *Spectroscopy of Polymers*, Elsevier, New York, 1999.
45 S. H. Kim and A. R. Lim, *Solid State Sci.*, 2022, **131**, 106927.